PAPER

Check for updates

Metal oxide heterostructures as multifunctional electrode materials for battery-type supercapacitors and oxygen evolution reactions

Urooj Ashfaq,†[a] Muhammad Nasir Hussain,†[ab] Abdul Naveed,[a] Irsa Tariq,*[ac] Muhammad Adil Mansoor, [ID][d] Sedat Yaşar, [ID][b] Talha Nisar, [ID][ef] Veit Wagner,[e] Amin Badshah*[ag] and Ali Haider [ID]*[ag]

This study demonstrates the successful synthesis of pristine Bi_2O_3, Co_3O_4, and Bi_2O_3/Co_3O_4 heterostructures for investigating their electrochemical energy storage and electrocatalytic performance. Among all the fabricated electrodes for battery-type supercapacitors, the Bi_2O_3/Co_3O_4 heterostructure exhibits a maximum specific capacitance of 2998 F g^{-1} at 1 A g^{-1} due to the synergistic interaction between the pristine Bi_2O_3 and Co_3O_4 nanoparticles. Furthermore, the Bi_2O_3/Co_3O_4 heterostructure was employed as an asymmetric supercapacitor device with a specific capacitance of 237 F g^{-1} at 2 A g^{-1}. The device exhibited a remarkable energy density of 32.97 Wh kg^{-1} at a power density of 0.333 kW kg^{-1}. Additionally, the Bi_2O_3/Co_3O_4 catalyst displayed increased oxygen evolution reaction rates result in both alkaline and neutral media with very low overpotentials of 464 mV and 153 mV at current densities of 50 mA cm^{-2} and 10 mA cm^{-2}, respectively. The values of Tafel slope, electrochemical surface area, and charge-transfer resistance confirmed the fast electrode kinetics and high density of active sites. The fabricated electrode exhibited long-term stability when tested for 24 hours under chronoamperometry. These findings indicate that the Bi_2O_3/Co_3O_4 heterostructure is an attractive electrode material for energy storage and generation applications.

Introduction

The growing demand for clean energy and the intermittent nature of renewable energy sources have sparked huge efforts to develop sustainable energy storage devices with high performance.[1–6] Of all the energy storage devices, supercapacitors have been considered as appealing candidates due to their fast charging capacity, high power density, and long cycle. Moreover, supercapacitors bridge the gap between conventional capacitors and batteries.[7–9] However, the low energy density of supercapacitors compared to those of batteries is a challenge that needs to be addressed.[10,11] Supercapacitors store charge through two different mechanisms depending on the type of electrode materials employed to fabricate the device. First, carbon-based materials store charge through the development of electrical double-layer capacitance (EDLC) at the electrode–electrolyte interface. Second, metal oxides store charge through the faradaic phenomenon.[1,12] Therefore, an electrode material with exceptional electrochemical characteristics is crucial to achieve enhanced performance of supercapacitor devices. Numerous metal oxides including Co_3O_4, Bi_2O_3, NiO, RuO_2, MnO_2, TiO_2, and V_2O_5 are promising electrode materials for supercapacitor applications.[13–20] Metal oxides have huge potential for supercapacitors with high specific capacitance, but their poor charge–discharge rates and low cyclic stability limit their practical applications. This limitation can be overcome by employing various strategies, including structural modification or composite fabrication with other materials.[21]

Co_3O_4 is a promising pseudocapacitive electrode material that is used widely in supercapacitors with low environmental impact and excellent theoretical capacitance.[22,23] The various morphologies of Co_3O_4 play an important role in the enhancement of capacitance.[24,25] Despite these efforts, Co_3O_4 suffers from low capacitance because of the limited availability of surface area and sluggish interfacial reaction kinetics. Additionally, the formation of Co_3O_4-based composites with other

[a]*Department of Chemistry, Quaid-i-Azam University, Islamabad, 45320, Pakistan. E-mail: irsatariq@chem.qau.edu.pk; aminbadshah@qau.edu.pk; ahaider@qau.edu.pk*

[b]*İnönü University, Faculty of Science and Art, Department of Chemistry, 44280, Malatya, Türkiye*

[c]*School of Materials Science and Engineering, Anhui University, Hefei, Anhui 230601, PR China*

[d]*Department of Chemistry, School of Natural Sciences (SNS), National University of Sciences and Technology (NUST), H-12, Islamabad, 44000, Pakistan*

[e]*School of Science, Constructor University, Campus Ring 1, 28759, Bremen, Germany*

[f]*Karlsruhe Institute of Technology (KIT), Institute for Applied Materials (IAM), Karlsruhe 76131, Germany*

[g]*Pakistan Academy of Sciences, 3-Constitution Avenue, Sector G-5/2, Islamabad 44000, Pakistan*

† U. A. and N. H. contributed equally to this paper.

materials, such as layered double hydroxides, metal oxides, carbonaceous materials, and conducting polymers, can significantly enhance the electrochemical performance by improving conductivity and facilitating charge-transfer kinetics.[26–28] These approaches demonstrate the potential of Co_3O_4-based materials for high-performance supercapacitors when integrated with other materials.[29,30] Additionally, Bi_2O_3 has emerged as an excellent electrode material that can be used to make a composite with Co_3O_4 due to its high conductivity, cost-effectiveness, environmental friendliness, and various oxidation states.[31,32] The excellent storage capacity of Bi_2O_3 is attributed to the existence of a faradaic redox transition between Bi^{3+} and Bi^0.[33,34] The Bi_2O_3/Co_3O_4 heterostructure has gained much interest for electrochemical energy storage because of its combined effect. The synergistic effect of the Bi_2O_3/Co_3O_4 heterostructure leads to excellent performance and stability compared to those of the individual components. The excellent performance of composite materials is attributed to their high surface area, high conductivity, and fast charge transfer in the composite material.[35,36] However, the Bi_2O_3/Co_3O_4 heterostructure has also been employed as a promising bifunctional electrocatalyst for the oxygen evolution reaction (OER) and hydrogen evolution reaction (HER) in overall water splitting. The composite has a modulated electronic structure compared to the individual parts, which increases the density of states at the Fermi level and lowers the rate determining step, reducing the overpotential and improving the charge-transfer kinetics. The synergistic effect between Co_3O_4 and Bi_2O_3 enhances the adsorption energies of oxygen and hydrogen species, promoting efficient reaction kinetics for OER and HER, respectively. This bifunctional characteristic makes the composite an appealing and cost-effective alternative candidate to noble metal-based electrocatalysts for water splitting.[37–40]

In this paper, we report the successful development of a multifunctional Bi_2O_3/Co_3O_4 heterostructure via the facile physical mixing of Bi_2O_3 and Co_3O_4 nanoparticles. The choice of physical mixing techniques has an advantage over chemicals because it provides direct interfacial contact between the pristine components, which promotes fast charge transfer, maintains independent redox-active sites, improves ion diffusion via the existence of high porosity, and provides a stable electroactive framework. Therefore, the composite delivered the highest specific capacitance and promising performance using the asymmetric device, making it a suitable material for energy storage systems. However, the excellent OER performance in alkaline and neutral electrolytes with high stability and low overpotential values revealed the potential for a robust and cost-effective bifunctional electrocatalyst. These features stand out in the Bi_2O_3/Co_3O_4 heterostructure, which is a strong candidate for hybrid energy storage and generation devices to promote efficient and clean energy solutions.

Experimental section

Materials

Bismuth(III) nitrate pentahydrate ($Bi(NO_3)_3 \cdot 5H_2O$, ≥98.0%), cobalt(II) nitrate hexahydrate ($Co(NO_3)_2 \cdot 6H_2O$, ≥98%), sodium sulfate (Na_2SO_4, ≥99.0%), sodium hydroxide (NaOH, ≥97.0%), ammonium hydroxide (NH_4OH, 32.0% NH_3 basis), ethanol (CH_3CH_2OH, ≥95.0%), polyvinyl alcohol [$(C_2H_4O)_n$, ≥99%], potassium hydroxide (KOH, ≥99.95%), carbon black (C, ≥99%), polyvinylidene fluoride (PVDF, ≥99%), and N-methyl-2-pyrrolidone (NMP, ≥99.7%) were purchased from Sigma Aldrich (USA) and used as received without further purification.

Synthesis of pristine Bi_2O_3, Co_3O_4 and Bi_2O_3/Co_3O_4 heterostructure

In a typical synthesis of Bi_2O_3 nanoparticles, a mixture of 25 mL of $Bi(NO_3)_3 \cdot 5H_2O$ and Na_2SO_4 was stirred under standard conditions. To this, 25 mL of NaOH solution was added, and the mixture was transferred to a Teflon-lined stainless-steel autoclave. The temperature was maintained at 120 °C for 2 hours. After that, the mixture was cooled to room temperature, and the yellow precipitate was collected via filtration. The precipitate was washed several times with water and ethanol and dried at 70 °C.[41] However, Co_3O_4 nanoparticles were prepared using the co-precipitation technique. The 60 mL of $Co(NO_3)_2 \cdot 5H_2O$ aqueous solution was mixed with 10 mL of NH_4OH (32%), and the pH of the solution was maintained at 11. The temperature of the mixture was increased to 80 °C for 1 hour and then cooled down to room temperature.[42] Finally, the mixture was centrifuged and annealed at 700 °C for 4 hours to obtain Co_3O_4 nanoparticles. The Bi_2O_3/Co_3O_4 heterostructure was obtained by physically mixing the already prepared solutions, where 10 mL solutions of each Bi_2O_3 and Co_3O_4 nanoparticle were separately sonicated for 30 minutes. Both solutions were mixed and ultrasonicated for 1 hour. The resulting mixture was centrifuged and dried to obtain the Bi_2O_3/Co_3O_4 heterostructure. A schematic illustration of the synthesis of the heterostructure is shown in Fig. 1.

Preparation of the polymer gel electrolyte

The PVA/KOH gel was employed as an electrolyte during the fabrication of an asymmetric supercapacitor (ASC). The electrolyte was synthesized using a solution chemistry method. In a typical synthesis, 1.5 g of PVA was mixed with 20 mL of distilled water and heated at 90 °C until the solution color reached a transparent and uniform viscous. Subsequently, the solution was cooled to room temperature, and 2 g of KOH dissolved in 10 mL of solvent was added, followed by stirring for 2 hours under ambient conditions. The obtained adhesive solution was transferred into a Petri dish and left for 24 hours for spontaneous drying.

Electrode fabrication for supercapacitor investigation

The electrode was fabricated using an active material deposited on nickel foam (NF) using the drop casting method. First, the nickel foam was activated by washing it with acetone, 3 M H_2SO_4, water and ethanol. A mixture of active material, conductive carbon, and PVF in a ratio of 8 : 1 : 1 was dispersed in NMP to prepare the slurry. The slurry was deposited on nickel foam with dimensions of 1 × 1 cm^2 and dried at 70 °C for 12 hours. The deposited mass on the nickel foam was
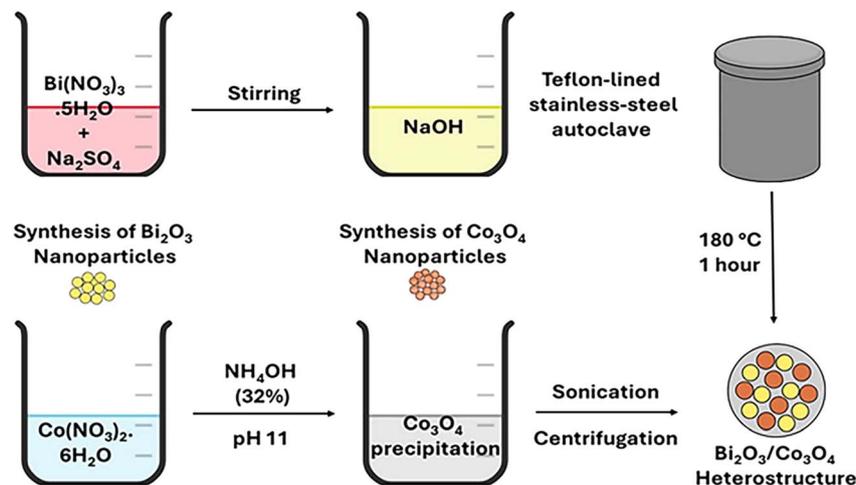
Fig. 1 Schematic of the synthesis of the Bi_2O_3/Co_3O_4 heterostructure.

approximately 1 mg $\pm$ 5%. All the electrochemical measurements were carried out using the Gamry workstation (Interface 101E). The specific capacitance was measured using eqn (1):[43]

$$C_{sp} = \frac{I \times \Delta t}{m \times \Delta V}, \tag{1}$$

where C_{sp} is in F g^{-1}, I denotes the current (A), m is the mass in grams, Δt is the discharge time in seconds, and ΔV is the potential window in volts.

Electrode fabrication for OER investigation

OER investigations were performed in alkaline and neutral media using 1 M KOH and 1 M sodium phosphate buffer (PBS) as electrolytes. Bi_2O_3, Co_3O_4, and Bi_2O_3/Co_3O_4 are used as working electrodes, platinum sheets as counter electrodes, and Ag/AgCl as reference electrodes. Linear sweep voltammetry (LSV) was employed to measure the OER activity. All measurements were iR-compensated and converted against a reversible hydrogen electrode (RHE) using the following Nernst equation:

$$E_{RHE} = E_{Ag/AgCl} + 0.0591 \times pH + 0.1976. \tag{2}$$

Cyclic voltammetry (CV) was performed in the non-faradaic region at scan rates ranging from 50 to 250 mV s^{-1} to estimate the electrochemical double-layer capacitance (C_{dl}). Stability tests were conducted via chronoamperometry at a constant potential of 50 mA cm^{-2} (basic pH) and 10 mA cm^{-2} (neutral pH) for 24 hours. Electrochemical impedance spectroscopy (EIS) was performed in the frequency range of 0.1–10^5 Hz with an alternative current (AC) amplitude of 10 mV.

Physical characterization

X-ray diffraction (XRD) spectra were obtained by employing a PANalytical X'pert diffractometer with Cu-Kα radiation (λ = 1.54 Å) over an angle range from 10° to 70°. The oxidation state of each element in the samples was determined by X-ray photoelectron spectroscopy (XPS) analysis using a PHI 5000 VersaProbe instrument. Scanning electron microscopy (SEM)

images were recorded using an FEI NOVA SEM-450 instrument, and the composition was determined using an X-ray energy dispersive (EDX) (INCAX-Act) spectrometer.

Results and discussion

The phase purities of the as-synthesized Bi_2O_3, Co_3O_4, and Bi_2O_3/Co_3O_4 heterostructures were determined using XRD, as shown in Fig. 2(a). The intense peaks in the XRD spectra indicate the crystalline nature of the nanomaterials. For Bi_2O_3, all the diffraction peaks matched well with the monoclinic phase (α) and JCPDS: 65-2366. There is no extra peak, which suggests that the material is indeed a single phase. For Co_3O_4, the peaks assigned to the crystal planes of (311), (400), (511), and (440) align with the face-centered cubic structure, corresponding to JCPDS: 42-1467. The presence of all peaks for Bi_2O_3 and Co_3O_4 confirmed the successful formation of the heterostructure, with no impurity peaks. The XPS analysis was carried out to find the exact oxidation state of each element present in the Bi_2O_3/Co_3O_4 heterostructure. The survey spectrum of the Bi_2O_3/Co_3O_4 heterostructure contains photoelectron and Auger peaks, which correspond to cobalt, oxygen, bismuth, and carbon, as shown in Fig. 2(b). The +3-oxidation state of Bi is confirmed in Bi_2O_3 by the binding energies of 160.8 and 166.2 eV for Bi 4f$_{7/2}$ and 4f$_{5/2}$, respectively, as Bi 4f indicates a doublet,[44] as presented in Fig. 2(c). The XPS spectrum of Co 2p demonstrates two peaks at binding energies of 779.9 and 795.1 eV, as shown in Fig. 2(d). The spin–orbit doublet 2p peaks are assigned to the tetrahedral and octahedral forms of Co^{2+} and Co^{3+} of the Bi_2O_3/Co_3O_4 heterostructure. The presence of satellite peaks in the higher binding energy regions of 2p$_{3/2}$ and 2p$_{1/2}$ confirmed the co-existence of Co(II) and Co(III) at the surface of the material, respectively. The binding energy difference of 15.2 eV is consistent with 2p$_{3/2}$ and 2p$_{1/2}$.[45]

The surface morphology of the prepared Bi_2O_3/Co_3O_4 heterostructure was investigated using SEM. SEM images of the Bi_2O_3/Co_3O_4 composite at different resolutions are shown in Fig. 3(a)–(c). The Bi_2O_3 has a flat rod shape, while Co_3O_4 exhibits
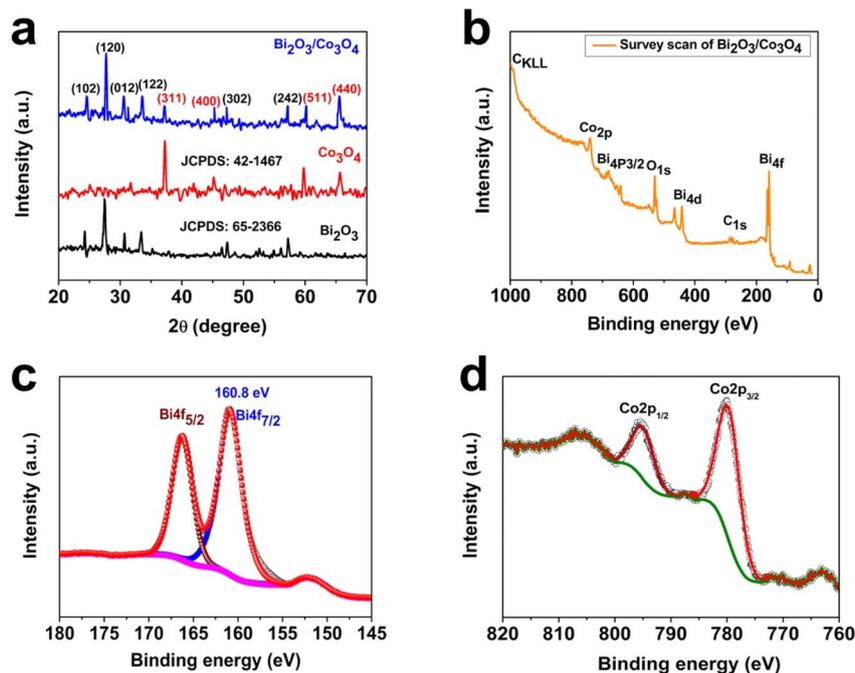
Fig. 2 (a) XRD spectra of thebBi$_2$O$_3$ (black), Co$_3$O$_4$ (red), and Bi$_2$O$_3$/Co$_3$O$_4$ (blue) heterostructures. XPS spectra of the Bi$_2$O$_3$/Co$_3$O$_4$ heterostructure: (b) survey scan, (c) Bi 4f, and (d) Co 2p.

spherical morphology with some agglomeration behaviors. EDX was performed to determine the elemental composition of each element in the Bi$_2$O$_3$/Co$_3$O$_4$ heterostructure. The EDX spectrum of the composite contains the peaks of Co, Bi, O, and C with no impurity peaks, which confirms the purity of the prepared material, as presented in Fig. S1. Moreover, the elemental mapping of the Bi$_2$O$_3$/Co$_3$O$_4$ heterostructure was conducted, indicating the homogeneous distribution of elements in the sample. The combined mapping image with each element image is illustrated in Fig. 3(d).

Electrochemical measurements

Electrochemical measurements of pristine Bi$_2$O$_3$, Co$_3$O$_4$, and Bi$_2$O$_3$/Co$_3$O$_4$ heterostructure materials were conducted to

investigate their potential for supercapacitors. The comparative CV profiles of all the prepared materials conducted at 10 mV s^{-1} in 5 M KOH are depicted in Fig. S2. The cyclic voltammetry (CV) profiles for pristine Bi$_2$O$_3$, Co$_3$O$_4$, and Bi$_2$O$_3$/Co$_3$O$_4$ heterostructure at various scan rates range from 10 to 100 mV s^{-1} in a potential window of −0.2 to 0.6 V by employing a 5 M KOH electrolyte, as shown in Fig. 4(a–c). The presence of a reversible redox pair contributes to the faradaic reaction that occurs at the surface of the electrode–electrolyte interface. A slight change in the redox peak position is observed, which can be due to an ion diffusion phenomenon and cause electrode polarization. The increase in peak current with an increase in scan rate indicated electron and ion transfer at the electrode. The Bi$_2$O$_3$/Co$_3$O$_4$ heterostructure demonstrates more storage capacity than the individual materials,

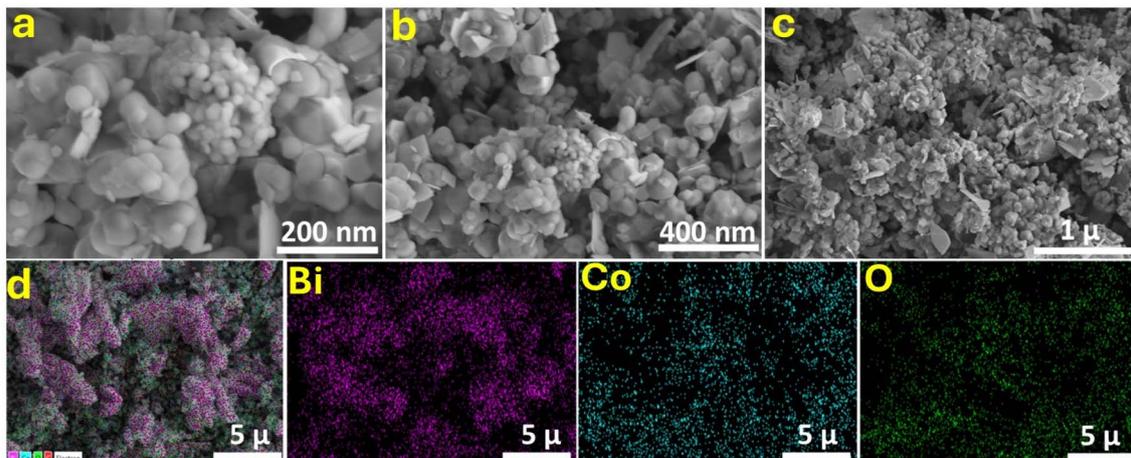Fig. 3 SEM images at different magnifications: (a)–(c) Bi$_2$O$_3$/Co$_3$O$_4$ composite, and (d) elemental mappings of the Bi$_2$O$_3$/Co$_3$O$_4$ heterostructure.
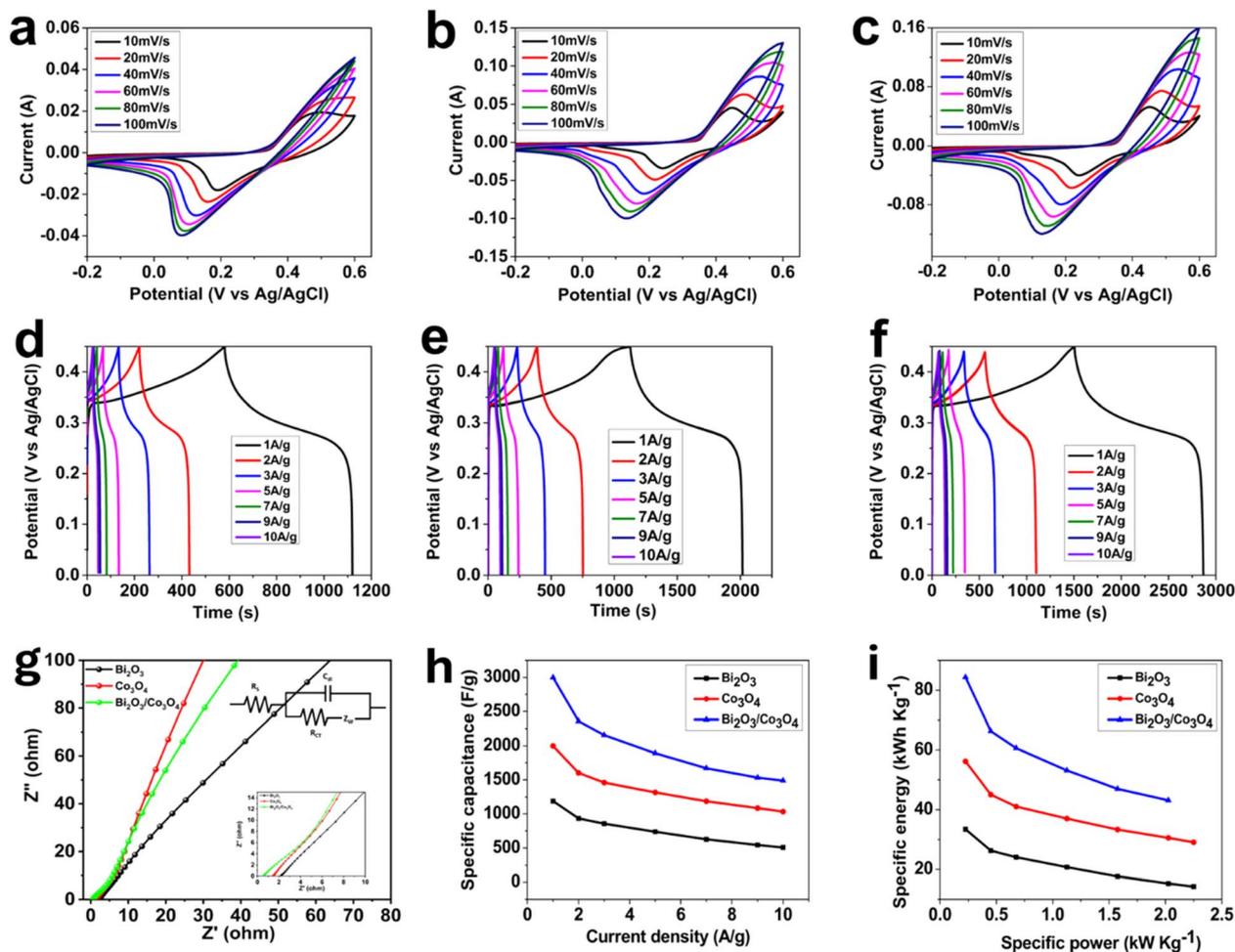
Fig. 4 CV profiles: (a) Bi_2O_3, (b) Co_3O_4, and (c) Bi_2O_3/Co_3O_4 heterostructure; GCD profiles: (d) Bi_2O_3, (e) Co_3O_4, and (f) Bi_2O_3/Co_3O_4 heterostructure; (g) EIS profiles of the synthesized nanomaterials; (h) current density *vs.* specific capacitance; and (i) Ragone plots.

as observed from the comparative CV profiles. This superior performance of the Bi_2O_3/Co_3O_4 heterostructure can be attributed to synergistic interfacial interactions between Bi_2O_3 and Co_3O_4. The formation of the heterojunction induces interfacial charge redistribution and a built-in electric field, which promotes faster electron transfer.[46] Simultaneously, strong Bi–O–Co electronic coupling and orbital hybridization modulate the electronic structure and optimize reaction kinetics. The mixed-valence nature of Bi_2O_3/Co_3O_4 provides redox buffering that stabilizes the Bi active sites during cycling, while the lattice mismatch at the interface introduces defects and oxygen vacancies that create additional electroactive centers. Together, these effects enhance charge-transfer kinetics and structural stability, thereby confirming the observed synergistic behavior.[47,48] Storage mechanisms based on plausible redox reactions[49,50] are presented using eqn (3) and (4).

$$Bi_2O_3 + 6OH^- \Leftrightarrow 2BiO_3^- + 3H_2O + 2e^- \quad (3)$$

$$Co_3O_4 + OH^- + H_2O \Leftrightarrow 3CoOOH + e^- \quad (4)$$
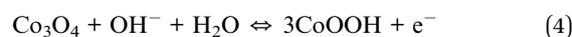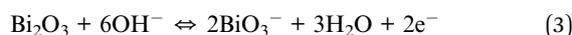
The galvanostatic charge–discharge (GCD) analysis was carried out for pristine Bi_2O_3, Co_3O_4, and Bi_2O_3/Co_3O_4 heterostructure in a potential window of 0–0.45 V at various current densities ranging from 1 to 10 A g^{-1}. The GCD profiles of all materials were conducted at different current densities in 5 M KOH, as shown in Fig. 4(d)–(f). The GCD profile shows a non-linear triangular shape, which is battery-type behaviour.[51] The presence of distinct redox plateaus suggests diffusion-influenced charge storage associated with reversible transition metal redox couples, which is characteristic of battery-type electrodes.[52] Among all the electrodes, the Bi_2O_3/Co_3O_4 heterostructure has the longest discharge time at all current densities compared to the pristine Bi_2O_3 and Co_3O_4 nanoparticles. The maximum specific capacitance delivered by the Bi_2O_3/Co_3O_4 heterostructure is 2998 F g^{-1} at 1 A g^{-1}, which outperforms pristine materials. The excellent capacitance performance of the composite is attributed to the synergy exhibited between all components. Synergy improves numerous electrochemical parameters, such as electroactive surface area, electrical conductivity, ion diffusion paths, and complete utilization of redox-active species. Moreover, an increase in current density

causes a gradual decrease in discharge time, which results in a reduction in specific capacitance. This trend arises at high current rates, where OH^- ions do not have enough time to permeate the inner active regions of the electrode, resulting in the partial utilization of active sites. However, heterostructure electrodes still demonstrate excellent rate capability in comparison to pristine counterparts, indicating robust and stable redox kinetics at high charge–discharge rates. These results indicate the strong potential of the Bi_2O_3/Co_3O_4 heterostructure for supercapacitor applications. A performance comparison of the Bi_2O_3/Co_3O_4 heterostructure with various reports is presented in Table S1. Different potential windows have been employed in CV and GCD analyses to avoid water splitting during the charging process.[53]

Nyquist plots were recorded for all fabricated electrodes over a frequency range of 0.1 Hz to 100 kHz, as depicted in Fig. 4(g). The depressed semicircle in the high frequency region reflects non-ideal charge-transfer behavior and surface heterogeneity, which is typically indicated using a constant phase element (CPE) rather than an ideal capacitor. In the low-frequency region, the line angle is less than 90° (i.e., deviating from a vertical capacitive line), indicating that the system does not exhibit purely ideal capacitive behavior. Instead, the slanted line suggests diffusion ion transport (Warburg impedance), which is characteristic of faradaic redox reactions coupled with ion intercalation/diffusion processes. A vertical line ($\sim$90°) corresponds to ideal capacitive charge storage, while a $\sim$45° Warburg slope represents semi-infinite diffusion. The intermediate angle observed here supports a mixed mechanism: surface capacitive adsorption/desorption combined with diffusion-controlled faradaic redox reactions.[54] This behavior is fully consistent with the non-linear GCD profiles and confirms that the electrode operates through combined pseudocapacitive and battery-type processes. The charge-transfer resistance (R_{ct}) values calculated for the pristine Bi_2O_3, Co_3O_4, and Bi_2O_3/Co_3O_4 heterostructure are 1.120 Ω, 1.091 Ω, and 0.901 Ω, respectively. The inset of the Nyquist plots focusing on a high frequency region (0–10 Ω) shows more details about the EIS and the model fitting of constant phase angle (CPE) with diffusion employed. The difference between R_{ct} and Warburg becomes more evident for each material by zooming into this range. A comparison of specific capacitance vs. current density demonstrates that capacitance decreases with an increase in current density, as depicted in Fig. 4(h). Ragone plots showed the highest specific energy density for the Bi_2O_3/Co_3O_4 heterostructure at the lowest current density compared to pristine materials, as presented in Fig. 4(i). The high value of specific energy density for the $Bi_2O_3/$

Co_3O_4 heterostructure indicates its promising potential as an electrode material for supercapacitor applications. Moreover, the materials are battery-type and directly influence Ragone plot interpretation. Battery-type materials generally deliver higher specific energy due to bulk faradaic reactions but at comparatively lower power density because ion diffusion limits fast charge–discharge.[55] The specific capacitance values calculated for all materials at different current densities are presented in Table 1.

Electrochemical investigation of an asymmetric device

The Bi_2O_3/Co_3O_4 heterostructure has been employed as a cathode material for ASC devices to test its practical viability. Activated carbon (AC) is used as an anode material to obtain a synergistic advantage. The graphical representation of the fabricated ASC is depicted in Fig. 5(a). The two different material-based electrodes offer distinct properties that ultimately enhance the storage capacitance of ASC devices. The use of the Bi_2O_3/Co_3O_4 heterostructure induces reversible faradaic reactions, which enhance energy storage through redox behaviour, and AC exhibits electrostatic charge accumulation, resulting in high power output and excellent cyclic stability. Therefore, the ASC device creates a balance between energy and power density to capitalize on the shortcomings of a symmetric device. The AC anode has a lower specific capacitance and is not able to store a charge equal to the Bi_2O_3/Co_3O_4 heterostructure. Therefore, the mass of the positive and negative electrodes must be balanced to obtain maximum efficiency. Eqn (5) used to balance the mass is given below:

$$\frac{m_+}{m_-} = \frac{C_- \Delta V_-}{C_+ \Delta V_+}. \tag{5}$$

The 3 mg of the Bi_2O_3/Co_3O_4 heterostructure and 10.6 mg AC were separately deposited on 2×2 cm^2 nickel foam used as substrates. The potential window optimization of the as-fabricated ASC is shown in Fig. S3. CV curves were obtained at 0–1 V at different scan rates employing 5 M KOH, as shown in Fig. 5(b). The GCD curves exhibit the same potential window with a triangular shape and great reversibility, as illustrated in Fig. 5(c). The specific capacitance values calculated were 237, 193, 148, 128, 110, and 106 F g^{-1} at 2, 3, 5, 7, 9, and 10 A g^{-1}, respectively. The R_{ct} and solution resistance (R_s) were evaluated, as depicted in Fig. 5(d). A depressed arc is observed in the high-frequency region, while a straight line is observed in the low-frequency region; moreover, the angle at the real axis is lower than 90°, indicating mass transfer and Warburg impedance. The R_{ct} and R_s values calculated are 21.29 and 0.490 Ω by fitting the model of the constant phase angle (CPE) with diffusion, respectively. The Ragone plot was used to calculate the energy and power density values of an as-fabricated ASC device, as shown in Fig. S4. The ASC device showed a maximum energy density of 32.97 Wh kg^{-1} with a power density of 0.333 kW kg^{-1} at 2 A g^{-1}. The device showed a capacity retention of 93.6% over 5000 cycles, indicating the excellent stability of the material, as shown in Fig. 5(e). Additionally, the ASC device was charged to

Table 1 Specific capacitance of all fabricated electrodes calculated from GCD analysis at various current densities

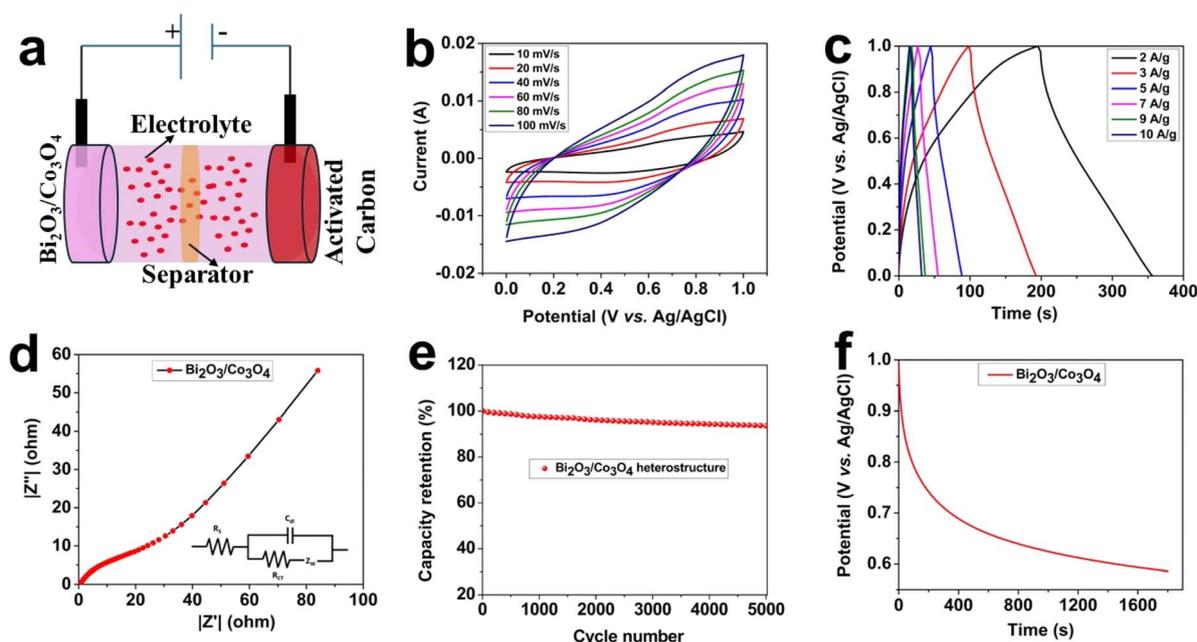| Current density (A g^{-1})	1	2	3	5	7	9	10
Bi_2O_3	1189	934	857	738	627.3	543.4	508
Co_3O_4	1998	1602	1459.3	1316	1186	1086	1034
Bi_2O_3/Co_3O_4	2998	2358.2	2155.3	1890	1671	1533	1488

Fig. 5 Electrochemical study of ASC: (a) graphical illustration of the ASC device, (b) CV curves at varying scan rates, (c) GCD profiles at different current densities, (d) Nyquist plot with fitted circuit model, (e) cycle stability, and (f) self-discharge test.

1 V, power was turned off and open circuit potential (OCP) observation was carried out against time, as shown in Fig. 5(f). The two-stage self-discharge behavior shows an initial rapid voltage drop to 0.6 V, followed by stabilization, which suggests the coexistence of different charge storage and loss mechanisms in the ASC. The fast initial decay is due to the redistribution of ions within porous electrodes, relaxation of the electric double layer, and discharge of weakly bound surface redox species. This process is driven by internal resistance and diffusion-controlled equilibration. After that, slower voltage decay indicates more stable faradaic charge storage, where deeper redox-active sites and more strongly adsorbed ions dominate, reflecting improved charge retention. For practical energy storage applications, this profile implies that although the device may experience some early voltage relaxation immediately after charging, it maintains relatively stable energy over longer resting periods. However, minimizing the initial rapid drop is important to enhance energy density and long-life performance in real-world devices.[56]

Electrochemical OER investigations

The electrocatalytic performance of the as-developed Bi_2O_3, Co_3O_4, and Bi_2O_3/Co_3O_4 materials was investigated for the OER in both alkaline (1 M KOH) and neutral (pH 7, 1 M PBS) electrolytes using LSV, Tafel analysis, CV, EIS, and chronoamperometry techniques. The overpotential (η) was determined at current densities of 50 mA cm^{-2} (alkaline) and 10 mA cm^{-2} (neutral). Fig. 6(a) depicts the LSV curves recorded in 1 M KOH at a scan rate of 10 mV s^{-1}, demonstrating that the Bi_2O_3/Co_3O_4 electrode achieved a current density of $\sim$327 mA cm^{-2} at 1.96 V vs. RHE, which significantly outperforms Co_3O_4

($\sim$163.7 mA cm^{-2}) and Bi_2O_3 ($\sim$138.4 mA cm^{-2}). The corresponding overpotentials at 50 mA cm^{-2} were 464 mV (Bi_2O_3/Co_3O_4), 524 mV (Co_3O_4), and 575 mV (Bi_2O_3). The higher current density and lower overpotential of Bi_2O_3/Co_3O_4 clearly demonstrate its superior catalytic performance compared to the other electrodes in the series.

This enhanced activity can be attributed to several synergistic factors. First, the improved redox chemistry arises from Bi_2O_3-mediated stabilization of catalytically active high-valent Co^{4+} species derived from Co_3O_4, which serve as primary active centers for OER via the CoO(OH) intermediate phase.[57] The stabilization of Co^{4+} in the Bi_2O_3/Co_3O_4 heterostructure is assigned to interfacial coupling and charge redistribution between both materials. The difference in Fermi levels causes electron transfer from Co_3O_4 to Bi_2O_3 upon heterostructure formation, resulting in hole accumulation at the interfacial Co sites and supporting the oxidation of Co^{3+} to Co^{4+} under OER potentials. In parallel, Bi–O–Co linkages promote orbital hybridization between Bi and Co states, which delocalizes the charge density and thermodynamically stabilizes the Co^{4+} species.[37] Second, the optimized electronic structure at the Bi_2O_3/Co_3O_4 heterointerface facilitates charge transfer and reduces the energy barrier for the critical OER step (*O $\rightarrow$ *OOH);[58] third, the improved mass transport is enabled by the three-dimensional nickel foam substrate, which provides a high surface area for active site exposure and efficient bubble release. The values of Bi_2O_3 are used as a reference, as already reported in our previous work.[59] Fig. 6(b) depicts the Tafel plot of the electrocatalysts in alkaline media, demonstrating that the Bi_2O_3/Co_3O_4 composite exhibits superior kinetic characteristics with a Tafel slope of 168.8 mV dec^{-1}, which is significantly lower than those of Co_3O_4 (277 mV dec^{-1}) and Bi_2O_3 (338.2 mV
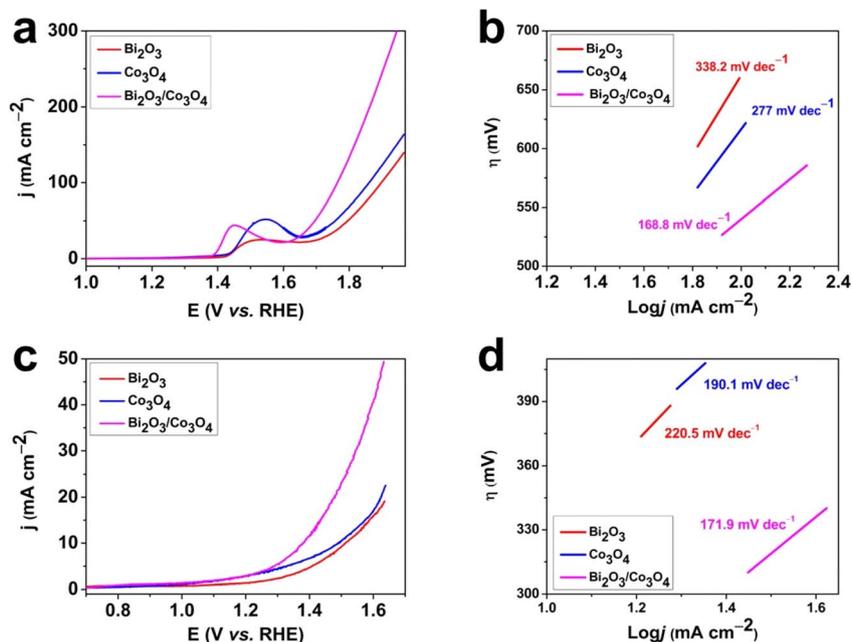
Fig. 6 (a) LSV curves for as-prepared electrocatalysts in alkaline media recorded for the OER at a scan rate of 10 mV s^{-1}, (b) Tafel plots for electrocatalysts in alkaline media, (c) LSV curves for as-prepared electrocatalysts in neutral media at a scan rate of 10 mV s^{-1}, and (d) Tafel plots for electrocatalysts in neutral media.

dec^{-1}). This inverse relationship between Tafel slope values and reaction rates confirms the enhanced OER kinetics of the composite material in alkaline media. When the OER measurements were performed in neutral (1 M PBS), the electrolyte and LSV profiles for all materials are presented in Fig. 6(c). The Bi_2O_3/Co_3O_4 electrode again showed superior activity, achieving a current density of ~49 mA cm^{-2} at 1.63 V vs. RHE, which is higher than that of the Co_3O_4 (~22.5 mA cm^{-2}) and Bi_2O_3 (~19.1 mA cm^{-2}). Moreover, Bi_2O_3/Co_3O_4 required only 153 mV at 10 mA cm^{-2}, which is lower than that of Co_3O_4 and Bi_2O_3 with 250 and 280, respectively. Furthermore, the reaction kinetics were quantitatively evaluated through Tafel analysis, as presented in Fig. 6(d). The measured Tafel slope for Bi_2O_3/Co_3O_4 is 171.9 mV dec^{-1}, which is lower than those of Co_3O_4 and Bi_2O_3, having 190.1 and 220.5 mV dec^{-1}. In comparison, the lower OER performance in neutral media compared to alkaline conditions arises from intrinsic mechanisms and kinetic limitations. At neutral pH, the OH$^-$ concentration is extremely low, so the reaction depends on water dissociation, which has a higher activation barrier than direct OH$^-$ adsorption in an alkaline electrolyte. Consequently, proton-coupled electron transfer (PCET) steps become sluggish, interfacial proton removal is hindered, and charge-transfer resistance increases due to lower ionic conductivity. In addition, the formation of highly active high-valent Co species is less favorable in neutral environments, limiting intrinsic catalytic activity. The Bi_2O_3/Co_3O_4 heterostructure mitigates these limitations through interfacial electronic coupling and charge redistribution, which facilitate Co^{3+}/Co^{4+} redox transitions and stabilize active sites. The built-in electric field at the heterointerface accelerates interfacial electron transfer, while Bi–O–

Co interactions promote water adsorption and activation, partially overcoming the water dissociation bottleneck. As a result, the heterostructure exhibits improved neutral-pH OER kinetics compared to pristine Bi_2O_3 and Co_3O_4.[60]

Furthermore, EIS measurements were conducted to further investigate the OER kinetics of the prepared electrodes. Nyquist plots were recorded in the frequency range of 0.1–10^5 Hz with an amplitude of 10 mV, which revealed distinct semicircular profiles for all electrodes in both alkaline and neutral media, as shown in Fig. 7(a) and (b). The Bi_2O_3/Co_3O_4 composite exhibited the smallest semicircle diameter among all tested electrodes, indicating a significantly lower R_{ct} compared to Bi_2O_3 and Co_3O_4. This reduced R_{ct} value demonstrates more favorable charge-transfer kinetics at the electrode–electrolyte interface, which directly correlates with the enhanced OER activity observed in polarization measurements. The quantitative R_{ct} values evaluated from equivalent circuit fitting further confirm the excellent electrocatalytic performance of the Bi_2O_3/Co_3O_4 composite, with the lowest resistance values recorded in both electrolyte media, as presented in Table S2. These EIS results provide additional evidence for the improved reaction kinetics and charge transport properties of the composite material, which is consistent with the outstanding OER performance demonstrated in previous electrochemical characterizations.

To evaluate the long-term stability of the Bi_2O_3/Co_3O_4 electrocatalyst, which demonstrated superior performance among all fabricated electrodes, chronoamperometric tests were conducted for 24 hours in both alkaline and neutral media, as depicted in Fig. 7(c) and (d). Under alkaline conditions, the electrode maintained a stable current density of 50 mA cm^{-2} at an applied potential of 1.694 V vs. RHE, while in
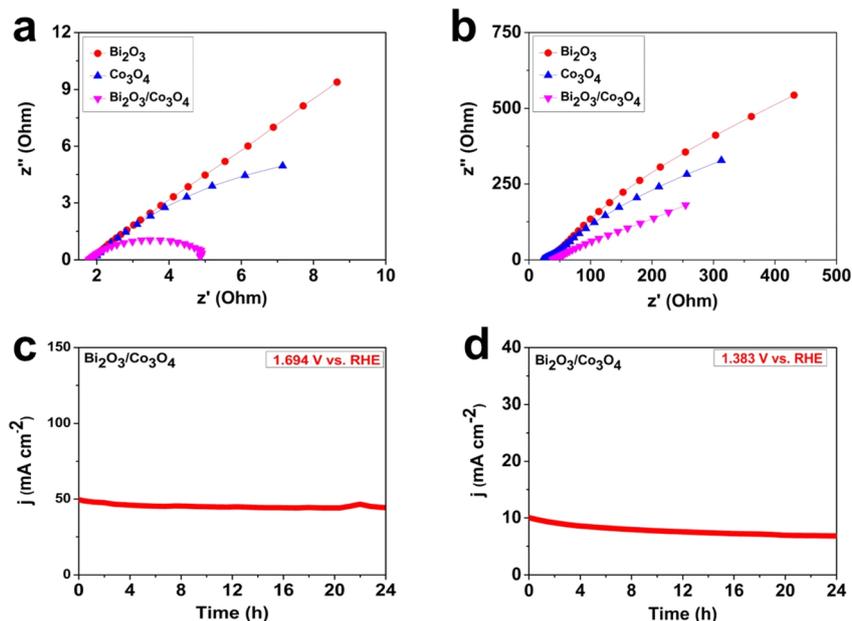
Fig. 7 (a) EIS of Bi_2O_3/Co_3O_4 in alkaline media, (b) EIS of Bi_2O_3/Co_3O_4 in neutral media, (c) chronoamperometry test of Bi_2O_3/Co_3O_4 in alkaline media, and (d) chronoamperometry test of Bi_2O_3/Co_3O_4 in neutral media.

neutral media, it sustained 10 mA cm^{-2} at 1.383 V *vs.* RHE. Remarkably, the electrocatalyst exhibited exceptional durability in both environments, showing only minimal current density fluctuations throughout the extended potentiostatic operation. These stability test results confirm the robust structural integrity and sustained catalytic activity of the Bi_2O_3/Co_3O_4 composite under continuous operation, highlighting its potential for practical applications in both alkaline and neutral electrochemical systems.

To further evaluate the electrocatalytic performance, CV was conducted in the non-faradaic region at scan rates ranging from 50 to 250 mV s^{-1} for the fabricated electrodes in both alkaline and neutral media. This analysis was used to determine the electrochemical surface area (ECSA) and double-layer capacitance (C_{dl}), which are critical indicators of the number of active sites and overall catalytic efficiency. The C_{dl} values were derived from the slope of the linear plot of anodic current density *vs.* scan rate. The CV curves of Bi_2O_3/Co_3O_4 in alkaline media exhibit well-defined capacitive behavior, as shown in Fig. S5(a). The corresponding C_{dl} plot reveals that Bi_2O_3/Co_3O_4 possesses a significantly higher C_{dl} (1.24 mF) than Bi_2O_3 (0.605 mF) and Co_3O_4 (0.703 mF), as illustrated in Fig. S5(b). The increased C_{dl} suggests a larger ECSA and a greater number of accessible active sites, which contribute to enhanced catalytic efficiency. A similar trend was observed in neutral media, where the C_{dl} values followed the order Bi_2O_3/Co_3O_4 (0.871 mF) > Co_3O_4 (0.454 mF) > Bi_2O_3 (0.28 mF), as shown in Fig. S5(c) and (d). The ECSA was calculated using the following equation:

$$ECSA = C_{dl}/C_s, \qquad (6)$$

where C_s represents the specific capacitance of a smooth monolayer (0.04 mF cm^{-2}). Since ECSA is directly proportional

to C_{dl}, a higher C_{dl} of Bi_2O_3/Co_3O_4 indicates a greater active surface area, facilitating improved electrocatalytic activity. Additionally, the roughness factor (RF), a key parameter influencing catalytic performance, was determined by the ratio of ECSA to the geometric surface area of the electrode. A higher RF signifies a more textured and porous electrode surface, which enhances electrocatalytic activity, particularly for the OER. Although the heterostructure provides electronic synergy, the optimal porosity and roughness arising from the mixing method could act as limiting mass-transport factors, particularly at higher current densities.[61] The OER performance metrics, including overpotential and Tafel slope, for all working electrodes in both alkaline and neutral media are summarized in Table S3. A comparative analysis of C_{dl}, ECSA, and RF for the tested electrodes, reinforcing the superior catalytic properties of the Bi_2O_3/Co_3O_4 composite, is shown in Table S4.

Conclusion

In summary, the synthesized pristine Bi_2O_3, Co_3O_4, and Bi_2O_3/Co_3O_4 heterostructure shows remarkable potential as an electrode material for high-performance supercapacitors and OER activity. The Bi_2O_3/Co_3O_4 heterostructure exhibits a maximum specific capacitance of 2998 F g^{-1} at 1 A g^{-1}, which is due to the synergistic interaction between Bi_2O_3 and Co_3O_4. Furthermore, the Bi_2O_3/Co_3O_4 heterostructure was employed for an asymmetric supercapacitor device with a specific capacitance of 237 F g^{-1} at 2 A g^{-1}. The ASC showed a remarkable energy density of 32.97 Wh kg^{-1} at a power density of 0.333 kW kg^{-1}. Additionally, the Bi_2O_3/Co_3O_4 catalyst displayed excellent OER results in both alkaline and neutral media with very low overpotentials of 464 mV and 153 mV at current densities of 50 mA cm^{-2} and 10

mA cm^{-2}, respectively. The fabricated electrode showed long-term stability when tested for 24 hours under chronoamperometry. The excellent stability and efficient overall water splitting further support the idea that the Bi$_2$O$_3$/Co$_3$O$_4$ heterostructure is a promising candidate for next-generation supercapacitors and electrocatalysts for sustainable energy technologies.

Conflicts of interest

There are no conflicts of interest to declare.

Data availability

All data generated or analyzed during this study are included in the published article and its supplementary information (SI). Raw data are available from the corresponding author upon reasonable request.

Supplementary information is available. See DOI: https://doi.org/10.1039/d5na01181g.

References

1 L. L. Zhang and X. Zhao, *Chem. Soc. Rev.*, 2009, **38**, 2520–2531.

2 P. Simon and Y. Gogotsi, *Nat. Mater.*, 2008, **7**, 845–854.

3 C. Liu, F. Li, L. P. Ma and H. M. Cheng, *Adv. Mater.*, 2010, **22**, E28–E62.

4 J. R. Miller and P. Simon, *Science*, 2008, **321**, 651–652.

5 A. S. Arico, P. Bruce, B. Scrosati, J.-M. Tarascon and W. Van Schalkwijk, *Nat. Mater.*, 2005, **4**, 366–377.

6 M. Kandasamy, S. Sahoo, S. K. Nayak, B. Chakraborty and C. S. Rout, *J. Mater. Chem. A*, 2021, **9**, 17643–17700.

7 Y. Wang, Z. Shi, Y. Huang, Y. Ma, C. Wang, M. Chen and Y. Chen, *J. Phys. Chem. C*, 2009, **113**, 13103–13107.

8 C. An, Y. Zhang, H. Guo and Y. Wang, *Nanoscale Adv.*, 2019, **1**, 4644–4658.

9 P. Bhojane, *J. Energy Storage*, 2022, **45**, 103654.

10 S. Jayakumar, P. C. Santhosh, M. M. Mohideen and A. Radhamani, *J. Alloys Compd.*, 2024, **976**, 173170.

11 M. F. Garcia, L. C. Arzuza, G. A. Neves, F. J. Loureiro, M. A. Morales, D. A. Macedo, H. L. Lira and R. R. Menezes, *Materials*, 2025, **18**, 413.

12 W. Yang, Z. Gao, J. Wang, B. Wang, Q. Liu, Z. Li, T. Mann, P. Yang, M. Zhang and L. Liu, *Electrochim. Acta*, 2012, **69**, 112–119.

13 R. Liang, Y. Du, P. Xiao, J. Cheng, S. Yuan, Y. Chen, J. Yuan and J. Chen, *Nanomaterials*, 2021, **11**, 1248.

14 B. Guo, Y. Gao, Y. Li, X. Sun, S. Chen and M. Li, *ACS Appl. Nano Mater.*, 2022, **5**, 7471–7480.

15 H. Zhang, H. Xie, D. Wang, Y. Xu, M. Yang, Z. Ai, Y. Shao, D. Shi, Y. Wu and X. Hao, *J. Colloid Interface Sci.*, 2025, **680**, 572–580.

16 R. Huang, J. Zhang, Z. Dong, H. Lin and S. Han, *ACS Appl. Energy Mater.*, 2023, **6**, 1673–1684.

17 J. Wu, F. Huang, T. Lee, Y. Yan, X. Pei, M. Wang, S. Gao, S. Guo, X. Pan and P. Wang, *ACS Appl. Energy Mater.*, 2022, **5**, 6962–6969.

18 X. Zhang, Y. Yang, P. Jia, S. Li, J. Su, S. Lv, Y. Sun, R. Liu, Y. Xu and W. K. Pang, *J. Power Sources*, 2025, **644**, 237117.

19 S. A. Mane, A. A. Kashale, G. P. Kamble, S. S. Kolekar, S. D. Dhas, M. D. Patil, A. V. Moholkar, B. R. Sathe and A. V. Ghule, *J. Alloys Compd.*, 2022, **926**, 166722.

20 D. Majumdar, M. Mandal and S. K. Bhattacharya, *ChemElectroChem*, 2019, **6**, 1623–1648.

21 D. D. Mohite, S. S. Chavan, P. E. Lokhande, K. B. Sutar, S. Dubal, U. Rednam, B. A. Al-Asbahi and Y. A. Kumar, *Mater. Today: Proc.*, 2024, **30**, 883.

22 C. Zhang, J. Xiao, X. Lv, L. Qian, S. Yuan, S. Wang and P. Lei, *J. Mater. Chem. A*, 2016, **4**, 16516–16523.

23 L. Yang, Q. Zhu, K. Yang, X. Xu, J. Huang, H. Chen and H. Wang, *Nanomaterials*, 2022, **12**, 4065.

24 R. S. Desai, V. S. Jadhav, S. R. Pardeshi, P. S. Patil, M. R. Hatshan, Y. A. Kumar and D. S. Dalavi, *Phys. Chem. Chem. Phys.*, 2025, **27**, 8098–8109.

25 K. P. Shwetha, C. Manjunatha, M. K. Sudha Kamath, Vinaykumar, M. G. R. Radhika and A. Khosla, *Appl. Res.*, 2022, **1**, e202200031.

26 Z. Wang, F. Tang, T. Li, X. Jiang, Q. Tian, M. Wang, J. Xu, L. Cui and J. Liu, *J. Power Sources*, 2025, **644**, 237118.

27 R. U. Amate, P. J. Morankar, M. K. Bhosale, A. M. Teli, S. A. Beknalkar and C.-W. Jeon, *Materials*, 2025, **18**, 2916.

28 A. Kumar, B. K. Satpathy, P. Goyal, R. Upadhyay, M. R. A. Kiapi, K. Jasuja, D. Menon and S. K. Misra, *J. Chem. Eng.*, 2025, **520**, 165685.

29 D. Kong, J. Luo, Y. Wang, W. Ren, T. Yu, Y. Luo, Y. Yang and C. Cheng, *Adv. Funct. Mater.*, 2014, **24**, 3815–3826.

30 C. Lu, L. Liu, Y. Yang, Y. Ma, Q. Luo and M. Zhu, *ChemNanoMat*, 2023, **9**, e202200537.

31 D. Gaikwad, R. Bobade, U. Nakate, P. Rosaiah, A. M. Tighezza, B. Lokhande and R. C. Ambare, *J. Mater. Sci.: Mater. Electron.*, 2024, **35**, 489.

32 M. K. Paliwal and S. K. Meher, *ACS Appl. Nano Mater.*, 2019, **2**, 5573–5586.

33 Y. Qiu, H. Fan, X. Chang, H. Dang, Q. Luo and Z. Cheng, *Appl. Surf. Sci.*, 2018, **434**, 16–20.

34 W. Zhu and D. Shen, *J. Energy Storage*, 2024, **79**, 110118.

35 G. Lakshmi Sagar, K. Brijesh, P. Mukesh, A. P. Hegde, A. Kumar, A. Kumar, K. S. Bhat and H. S. Nagaraja, *J. Electroanal. Chem.*, 2024, **975**, 118777.

36 I. B. Ahmed, M. Diaby, H. Nafati, A. Bardaoui, D. M. F. Santos, R. Chtourou and I. Ben Assaker, *Solid State Sci.*, 2024, **152**, 107537.

37 D. Gorylewski, F. Zasada, G. Słowik, M. Lofek, G. Grzybek, K. Tyszczuk-Rotko, A. Kotarba and P. Stelmachowski, *ACS Catal.*, 2025, **15**, 4746–4758.

38 Z. Hu, L. Hao, F. Quan and R. Guo, *Catal. Sci. Technol.*, 2022, **12**, 436–461.

39 R. Zhang, L. Pan, B. Guo, Z.-F. Huang, Z. Chen, L. Wang, X. Zhang, Z. Guo, W. Xu, K. P. Loh and J.-J. Zou, *J. Am. Chem. Soc.*, 2023, **145**, 2271–2281.

40 Q. T. Nguyen, U. T. Nakate, B. G. Ghule, S. Park, J. Choi, J. H. Park, J. R. Park, J.-H. Jang, D.-W. Kim and S. Park, *ACS Appl. Mater. Interfaces*, 2025, **17**, 12307–12316.

41 Z. A. Zulkifli, K. A. Razak and W. N. W. A. Rahman, *J. Phys.: Conf. Ser.*, 2018, **1082**, 012103.

42 S. Rajendiran, M. Chellasamy, H. Pitchai Sali Mohamed, M. Anbazhagan, S. Marimuthu and U. Sekar, *Nanotechnol. Environ. Eng.*, 2025, **10**, 43.

43 H. Sun, J. Pan, X. Yan, W. Shen, W. Zhong and X. Cheng, *Ceram. Int.*, 2019, **45**, 24802–24810.

44 H. M. Danamah, T. M. Al-Hejri, V. V. Jadhav, T. A. J. Siddiqui, S. F. Shaikh, A. u. H. S. Rana and R. S. Mane, *J. Power Sources*, 2025, **652**, 237301.

45 J. Li, H. Lin, Z. Ai, H. Feng, Y. Li, J. Xu and H. Xie, *J. Energy Storage*, 2025, **107**, 115041.

46 J.-h. Zhang, P.-j. Zhu, Y.-z. Liu, X.-r. Zhu, Y.-f. Li and C.-M. Chen, *J. Energy Storage*, 2025, **112**, 115543.

47 Y. Li, X. Zhu, X. Zhang, J. Zhang and Y. Liu, *J. Energy Storage*, 2025, **129**, 117351.

48 S. Balasundari, S. Jayasubramaniyan, P. Thangavel, M. Vithiya, T. Rani, P. A. Rayjada, N. Satyanarayana and P. Muralidharan, *ACS Appl. Eng. Mater.*, 2023, **1**, 606–615.

49 S. Azhar, K. S. Ahmad, I. Abrahams, W. Lin, R. K. Gupta, A. Nadeem and S. M. Attia, *Mater. Chem. Phys.*, 2025, **342**, 130944.

50 X. Zhang, Y. Yang, P. Jia, S. Li, J. Su, S. Lv, Y. Sun, R. Liu, Y. Xu and W. K. Pang, *J. Power Sources*, 2025, **644**, 237117.

51 Y. Liu, N. Fu, G. Zhang, M. Xu, W. Lu, L. Zhou and H. Huang, *Adv. Funct. Mater.*, 2017, **27**, 1605307.

52 Y. Tong, X. Liu, D. Qi and B. Chi, *J. Energy Storage*, 2024, **97**, 112798.

53 M. N. Hussain, A. Naveed, M. Sohail, M. D. Khan, S. G. Hickey, N. Ullah, I. Ahmad, A. Haider and S. M. Shah, *ACS Appl. Eng. Mater.*, 2025, **3**, 1315–1326.

54 J. E. S. Fonsaca, C. E. Lima, K. S. B. Martins, S. H. Domingues and C. J. S. de Matos, *Langmuir*, 2024, **40**, 21442–21452.

55 Y. Li, X. Zhu, X. Zhang, J. Zhang and Y. Liu, *J. Energy Storage*, 2025, **129**, 117351.

56 L. Song, W. Hou, H. Qiao, Q. Liu, J. Zhang, W. Zhang, D. Xiao and Q. Zhang, *J. Mater. Chem. A*, 2026.

57 D. Gorylewski, F. Zasada, G. Słowik, M. Lofek, G. Grzybek, K. Tyszczuk-Rotko, A. Kotarba and P. Stelmachowski, *ACS Catal.*, 2025, **15**, 4746–4758.

58 C. Stumm, M. Bertram, M. Kastenmeier, F. D. Speck, Z. Sun, J. Rodríguez-Fernández, J. V. Lauritsen, K. J. Mayrhofer, S. Cherevko and O. Brummel, *Adv. Funct. Mater.*, 2021, **31**, 2009923.

59 I. Tariq, A. Ali, A. Haider, W. Iqbal, M. A. Asghar, A. Badshah, M. A. Mansoor, T. Nisar, V. Wagner and S. M. Abbas, *Energy Technol.*, 2024, **12**, 2301504.

60 Y. Dong and S. Komarneni, *Small Methods*, 2021, **5**, 2000719.

61 V. M. Nikolić, K. M. Dimić-Mišić, S. L. Maslovara, D. P. Popović, M. N. Gigov, S. S. Krstić and M. P. Marčeta Kaninski, *Catalysts*, 2026, **16**, 98.